Journal of Rock Mechanics and Geotechnical Engineering 18 (2026) 4050–4063

Contents lists available at ScienceDirect

Journal of Rock Mechanics and Geotechnical Engineering

journal homepage: www.jrmge.cn

Full Length Article

Characterizing particle crushing behavior of dry granular soils by acoustic emission

Wenli Lin [a,b,c], Shuyu Tian [c,d], Deqi He [a], Xiao Kang [c,d], Yuhang Chen [a], Ang Liu [a,*], Maqsood Zain [e], Junichi Koseki [f]

[a] Department of Geological Engineering, Nanjing Tech University, Nanjing, 211800, China
[b] Department of Civil and Environmental Engineering, The Hong Kong Polytechnic University, Hong Kong, China
[c] School of Transportation, Southeast University, Nanjing, 211189, China
[d] Advanced Ocean Institute of Southeast University, Southeast University, Nanjing, 211189, China
[e] School of Civil and Environmental Engineering, National University of Sciences and Technology (NUST), Islamabad, 44000, Pakistan
[f] Department of Civil Engineering, The University of Tokyo, Tokyo, 113-8656, Japan

ARTICLE INFO

Article history:
Received 6 March 2025
Received in revised form
3 June 2025
Accepted 10 July 2025
Available online 29 November 2025

Keywords:
Granular materials
Particle crushing
Acoustic emission (AE)
Frequency response
Particle damage behavior

ABSTRACT

This study investigates particle crushing mechanisms in granular soils during shearing through staged triaxial compression experiments performed at prescribed axial strains and varying confining stresses, integrating a high-performance acoustic emission (AE) measurement system. The study analyzed particle crushing-related parameters using grain size distribution (GSD)-based indices (relative breakage index B_r and its rate ΔB_r) and AE-based parameters (high-frequency AE hits D_{AE}^{H} and hit rates R_{AE}^{H}). The results confirm the feasibility of high-frequency AEs (>100 kHz) in comprehensive quantification of particle crushing, with a strong linear relationship observed between D_{AE}^{H} and B_r. Significant particle crushing occurs within the initial 5 % of axial strain, which correlates with the yielding and peak-stress phases. This process yields fragments with a size range of 0.425–2 mm. Increased confining stresses result in a steady rise in B_r and D_{AE}^{H}, suggesting that large strains are required for stable particle grading. The evolution trends of different high-frequency AE ranges reveal a shift to complex crushing mechanisms, such as particle abrasion/grinding and corner breakage/particle splitting, highlighting the role of stress and strain levels in influencing particle damage behavior.

1. Introduction

In recent decades, significant advancements in both experimental and numerical methods have deepened our understanding of particle crushing mechanisms in granular materials. Particle crushing alters key material characteristics, such as particle shape, surface roughness, and grain size distribution (GSD), and is a complex process involving several distinct damage mechanisms, in terms of particle abrasion/grinding, corner breakage, and catastrophic splitting (Nakata et al., 2001). The nature and extent of these mechanisms are influenced by both internal and external factors. Internal factors mainly refer to the material's intrinsic properties (e.g. mineralogical composition, morphology and angularity characteristics, initial void ratio and gradation, and particle defects (e.g. intra-particle porosity), etc.). The external causation (or extrinsic factors) predominantly encompasses applied loading conditions, such as the stress path and confining pressure, strain rate dependency, thermo-chemical environment, and boundary constraint effects, among others (Lade et al., 1996; Indraratna et al., 1998; Nakata et al., 2001; Coop et al., 2004; Altuhafi and Coop, 2011; Yu, 2017a, b, c; Yu, 2017a, b, c, 2018; Yao et al., 2021a, b, 2023, 2024; Yao and Li, 2023; Li et al., 2024, 2025). Through one-dimensional compression tests, Nakata et al. (2001) observed that the transition from uniform to well-graded assemblies led to a shift in the nature of particle crushing: from sudden catastrophic splitting to gradual splitting of smaller particles, asperity breakage, and surface grinding. In contrast, Altuhafi

* Corresponding author.
E-mail address: fuxiao@njtech.edu.cn (A. Liu).

Peer review under responsibility of Institute of Rock and Soil Mechanics, Chinese Academy of Sciences.

https://doi.org/10.1016/j.jrmge.2025.07.039

and Coop (2011) found that non-uniformly graded specimens experienced less breakage, with larger particles primarily undergoing asperity damage and minimal particle splitting.

In addition to experimental studies, numerical and theoretical simulations have provided valuable insights into particle damage mechanisms upon loading. Bolton et al. (2008) conducted discrete element method (DEM) simulations on uniformly graded materials under compression, revealing a progression of damage: initial asperity breakage, followed by grain splitting during material yielding, and, at higher stress levels, both asperity damage and particle splitting across all grain sizes. Peng et al. (2022) demonstrated through simulations that the dominant breakage mode in crushable sands during pile penetration, whether full particle fracture or corner breakage, is governed by initial particle shape. However, the current understanding of how these mechanisms interact under varying stress–strain conditions remains qualitative, rendering the process inadequately understood.

Particle crushing has profound implications for soil mechanical behavior, manifested as the suppression of dilatancy, reductions in friction angles and permeability, and modification to the critical state line (Lade et al., 1996, 2010; Bandini and Coop, 2011; Yu, 2017a, b, c, 2018). To quantify these effects, numerous indices have been developed. Traditional approaches often focus on particle gradation changes at specific sizes (Lee and Farhoomand, 1967; Marsal, 1967; Hardin, 1985; Nakata et al., 1999) or variations in particle surface area (Miura and O-Hara, 1979; Nakata et al., 2001). Among these, the relative breakage index (B_r), introduced by Hardin (1985), remains the most widely adopted. Further exploration has incorporated fractal and energy theories, frequently in conjunction with the relative breakage index (B_r), to quantify particle crushing (Mandelbrot, 1983; Turcotte, 1986; Tyler and Wheatcraft, 1992; McDowell et al., 1996).

Based on the above-mentioned indices, methods such as sieving tests, digital Image correlation (DIC), and computed tomography (CT) have been employed to analyze changes in particle gradation or morphology. These methods have facilitated numerous studies examining the correlation between particle crushing-related indices (e.g. B_r) and macro-state parameters (e.g. energy consumption). For example, Miura and O-Hara (1979) established a correlation between changes in particle surface area and plastic work per unit volume in monotonic and cyclic triaxial tests. Similarly, Xiao and Liu (2017) introduced an exponential model correlating particle crushing, defined by a modified relative breakage based on the median particle size D_{50}, with plastic work per unit volume. Lade et al. (1996) used a hyperbolic model to correlate particle crushing (based on D_{10}, which indicates that 10 % of particles have sizes below this diameter) with total energy input per unit volume. Hu et al. (2011) developed another hyperbolic model linking modified B_r to plastic work per unit volume based on fractal grading. Liu and Zou (2013), Liu et al. (2014), Kong et al. (2016), and Yu (2017c, 2018) applied similar hyperbolic models to connect B_r with plastic work in both monotonic and cyclic triaxial tests. These models have proven useful in quantifying particle crushing, though they face challenges in isolating specific energy contributions to particle crushing from total specimen energy, which includes both crushing and non-crushing energy inputs.

This challenge raises an important question: how can particle crushing-related parameters (e.g. specific particle crushing energy) be effectively isolated from macro-state parameters (e.g. total specimen energy) to enable more accurate interpretations of particle crushing? This gap underscores the need for further investigation and the development of advanced techniques for distinguishing between different micro-mechanical behavior contributions.

Recent advancements in acoustic emission (AE) and computational techniques offer promising solutions to the above-mentioned issues. AE detects elastic waves stemming from micro-mechanical behaviors, such as particle crushing and rearrangement in granular soils, providing insights into material deterioration, failure mechanisms, and particle-interaction localization (Lei et al., 2004; Kundu, 2014; Manuello et al., 2019; Lin et al., 2021). AE parameters, such as hit (rate), have been shown to correlate strongly with particle interaction-induced inelastic strain, making AE a powerful tool for tracking particle interactions during shearing (Mao et al., 2018, 2025; Smith and Dixon, 2019; Lin et al., 2019, 2020a, b, 2024a, b, 2025; Li and Smith, 2025). Moreover, recent studies have identified the critical role of frequency-dependent AE signatures in the characterization of distinct particle-interaction mechanisms. (Dagois-Bohy et al., 2010; Michlmayr and Or, 2014; Mao and Towhata, 2015; Lin et al., 2019, 2025; Liu et al., 2022). Lin et al. (2019) found that AE signals from particle rearrangement are typically below 100 kHz, in contrast to those from particle crushing, which occupy a distinctly higher frequency range. On this basis, Lin et al. (2025) demonstrated a strong mathematical correlation between high-frequency AE (>100 kHz) parameters and the B_r index, enabling the identification of distinct trends in particle crushing rates based on failure modes, such as “barreling” or “shear banding”.

However, the study by Lin et al. (2025) was conducted under conditions with minimal particle crushing, using silica sands with a small median particle size (D_{50} = 0.471 mm) and low confining stresses (up to 600 kPa). This presents a key limitation for the utility of high-frequency AE parameters in quantifying extensive particle crushing. Moreover, no staged experiments were conducted to validate the use of AE for the comprehensive quantification of particle crushing. These limitations highlight the need for further research to explore the robustness of AE techniques under conditions that induce substantial particle crushing.

To address these gaps, the present study presents staged experimental results from a program of triaxial compression tests on silica sands with larger particle sizes and higher confining stresses. This study aimed to assess the capability of frequency-dependent AE parameters for comprehensively quantifying substantial particle crushing and clarifying the underlying mechanisms. This was achieved by correlating these crushing characteristics with AE signal frequencies, thereby providing deeper insight into the dynamics of granular soils under stress.

2. Experimental setup

2.1. Testing materials and apparatus

In a previous study, silica sand No. 5 (with a mean particle size of 0.471 mm) was selected as the testing material to demonstrate the capability of AE techniques in detecting subtle changes in particle crushing (Lin et al., 2025). To further assess the applicability of AE in quantifying substantial particle crushing during the shear process, silica sand No. 3 was selected for this study. Silica sand No. 3 shares the same mineral composition as silica sand No. 5 but has larger grain sizes, making it suitable for examining more pronounced crushing effects. Both sands were sourced from Gifu Prefecture, Japan, and provided by Takeori Co., Ltd. in Japan.

Fig. 1 presents the grain size distribution (GSD) curve of the sands prior to testing, revealing a poor gradation. Fig. 2 shows a microscopic image and laser scan of silica sand No. 3, highlighting its angular and rough surface with abundant asperities, which are expected to contribute to more substantial particle crushing in terms of asperity abrasion and particle gridding. The basic physical

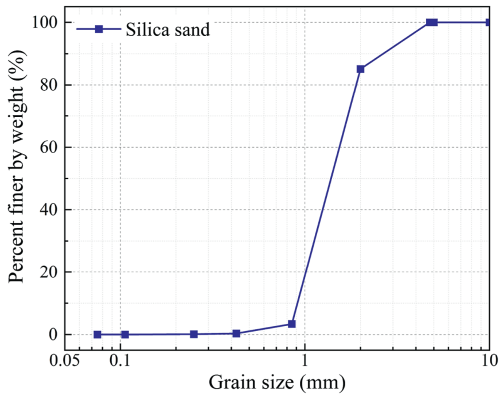

Fig. 1. GSD of tested silica sand No.3.

properties of the tested sands, including the maximum and minimum void ratios and specific gravity, were measured following the standards set by the Japanese Geotechnical Society (JGS 0111, 2015; JGS 0131, 2015; JGS 0161, 2015), with the results summarized in Table 1.

The soil specimen, with a size of 50 mm in diameter and 100 mm in height, was prepared into a 0.5 mm latex membrane using air pluviation from a certain height. This approach allows for the achievement of a relatively homogeneous specimen with the initial relative density maintained at around 85 %. The specimen was then subjected to isotropic loading to a target confining stress level, followed by an isotropic compression for 30 min, under dry conditions. The triaxial tests were conducted using a modified conventional apparatus featuring a low-friction, movable sled on the bottom pedestal (Fig. 3). This sled was capable of linear movement in two perpendicular directions and 360° in-plane rotation. Given the authors' interest in the study of shear banding using AE source locating technique (Lin et al., 2021), the sled was set to move laterally during the test in this study, as indicated in Fig. 3c. This setting facilitates shearing along the shear band without the lateral restraint imposed by a fixed base pedestal. The axial loading is servo-controlled by an AC servo-motor, and a constant loading rate of 1 mm/min was selected. The tests were terminated at different prescribed axial strain (ε_a) levels from 5 % to 30 % by a 5 % increment, to provide stage-experimental results of particle crushing for feasibility validation of the AE technique. Details regarding the testing program are listed in Table 2.

Measurements of the applied axial load, axial displacement, and confining pressure were obtained using a load cell, an axial linear displacement transducer, and a pressure transducer, respectively.

Table 1
Basic physical properties of tested silica sands No. 3.

G_s	d_{50} (mm)	C_u	C_c	e_{max}	e_{min}
2.632	1.39	1.69	0.9	0.988	0.691

2.2. AE measurement system

A high-performance AE measurement system, depicted in Fig. 3b, was utilized in this study. The system was composed of eight R-CAST 304A piezoelectric sensors coupled with four Model A1201 main amplifiers (Fuji Ceramics Corporation, Japan), a National Instruments PXIe-6366 data logger, and a dedicated computer. The AE sensors exhibit a sensitivity of 115 dB ± 3 dB (ref. 0 dB = 1 V/m/s) across a broad frequency range (10 kHz–5 MHz), with a resonant peak at 300 kHz. Each sensor integrates a field-effect transistor (FET) head amplifier (20 dB ± 2 dB gain) and connects to the main amplifier, providing 53 dB ± 3 dB gain, resulting in a 55 dB sensitivity enhancement over conventional systems. The AE sensor calibration data, as shown in Fig. 4a, revealed frequency-dependent sensitivity variations, with the minimum sensitivity (85 dB at ~90 kHz) still matching conventional sensors' peak performance. The NI PXIe-6366 data logger features eight simultaneous analog inputs with a 2 million samples/sampling rate, sufficient to resolve AE signals up to 1 MHz based on the Nyquist–Shannon criterion. AE signals associated with particle-scale interactions (e.g. rearrangement or crushing) exhibited peak frequencies reaching 700 kHz (Lin et al., 2019). Consequently, a sampling rate of 2 Millon Samples/s was deemed sufficient for reliable detection. The AE sensors were adhesively mounted in a four-layer configuration on the membrane surface near the specimen's end section (Fig. 3d), with aluminum shim plates ensuring optimal acoustic coupling. Complete system specifications are tabulated in Table 3, with additional methodological details available in Lin et al. (2025).

A typical AE waveform, along with its relevant parameters, is shown in Fig. 4b. To effectively discriminate the signals, a threshold of 0.03 V (i.e. 29.5 dB, referenced to 0 dB = 1 mV/(m s)) was applied. This threshold was selected based on the voltage level generated by electrical and ambient noise, which ranged from −0.01 V to 0.01 V (i.e. 20 dB, referenced to 0 dB = 1 mV/(m s)). An AE hit refers to a signal that exceeds the threshold, with its peak recorded as the amplitude. The dominant frequency was identified

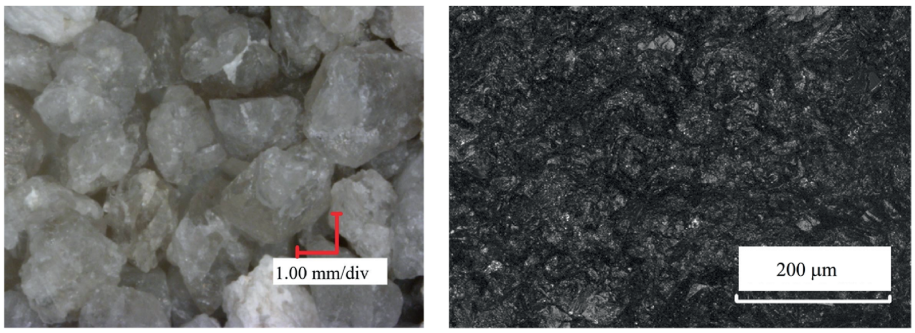

Fig. 2. (a) A microscopic image; and (b) A laser illustration of the tested silica sand No. 3.

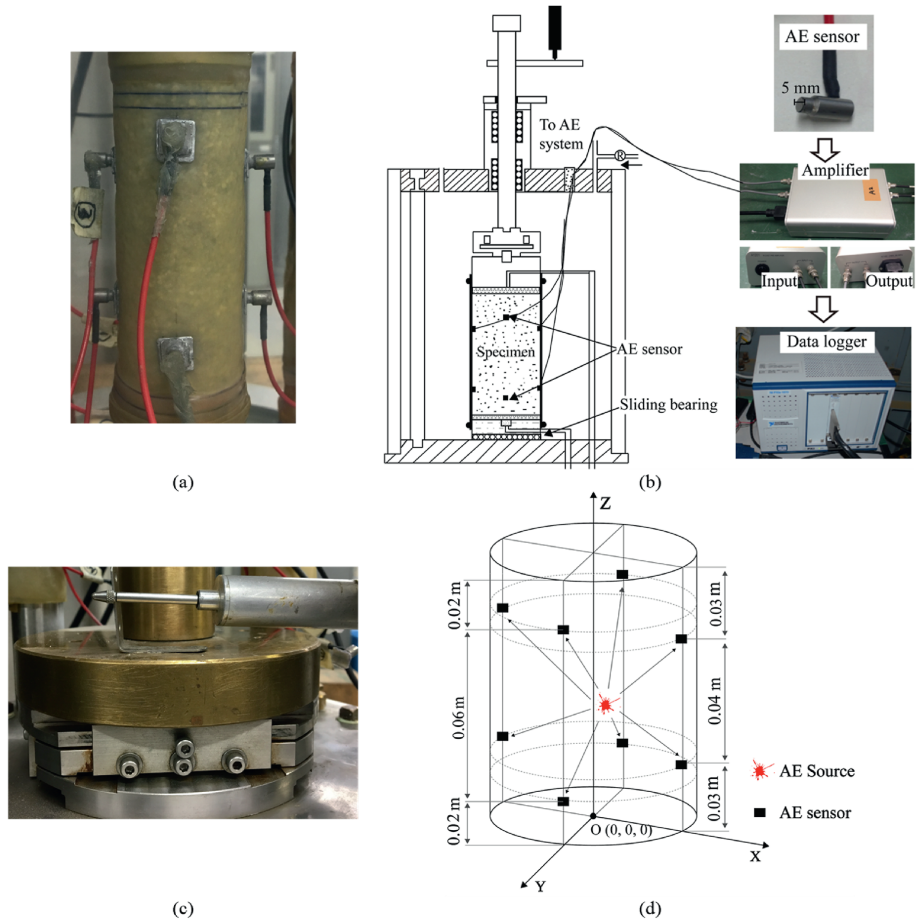

Fig. 3. (a) Soil specimen attached with AE sensors; (b) Schematic diagram of triaxial apparatus integrated with AE monitoring; (c) Low-friction movable sled on the bottom pedestal; and (d) Schematic of AE sensor layout and coordinate during compression.

Table 2
Testing program of silica sand No.3 subjected to drained triaxial compression.

Testing item	Specimen size, $D \times H$ (mm × mm)	Relative density (%)	Prescribed axial strain (%)	Confining stress(kPa)	Loading rate (mm/min)
S3-100-5	48 × 101.3	85.7	5	100	1
S3-100-10	48 × 101.7	84.8	10	100	
S3-100-15	48 × 101.7	84.4	15	100	
S3-100-20	48 × 101.5	85.2	20	100	
S3-100-25	48 × 101	86.2	25	100	
S3-100-30	48 × 101.6	84.3	30	100	
S3-400-5	48 × 101.5	85.2	5	400	
S3-400-10	48 × 101.5	85.7	10	400	
S3-400-15	48 × 101.1	86.4	15	400	
S3-400-20	48 × 101.3	85.9	20	400	
S3-400-25	48 × 101	86.9	25	400	
S3-400-30	48 × 101.3	86.2	30	400	
S3-800-5	48 × 101.9	83.8	5	800	
S3-800-10	48 × 101.2	86.4	10	800	
S3-800-15	48 × 101.6	85	15	800	
S3-800-20	48 × 101.1	86.9	20	800	
S3-800-25	48 × 101.7	84.7	25	800	
S3-800-30	48 × 101.3	86.1	30	800	
S3-1600-5	48 × 101.8	84.3	5	1600	
S3-1600-10	48 × 101.7	84.7	10	1600	
S3-1600-15	48 × 101.8	84.3	15	1600	
S3-1600-20	48 × 101.2	86.4	20	1600	
S3-1600-25	48 × 101.6	85	25	1600	
S3-1600-30	48 × 101.3	86.1	30	1600	

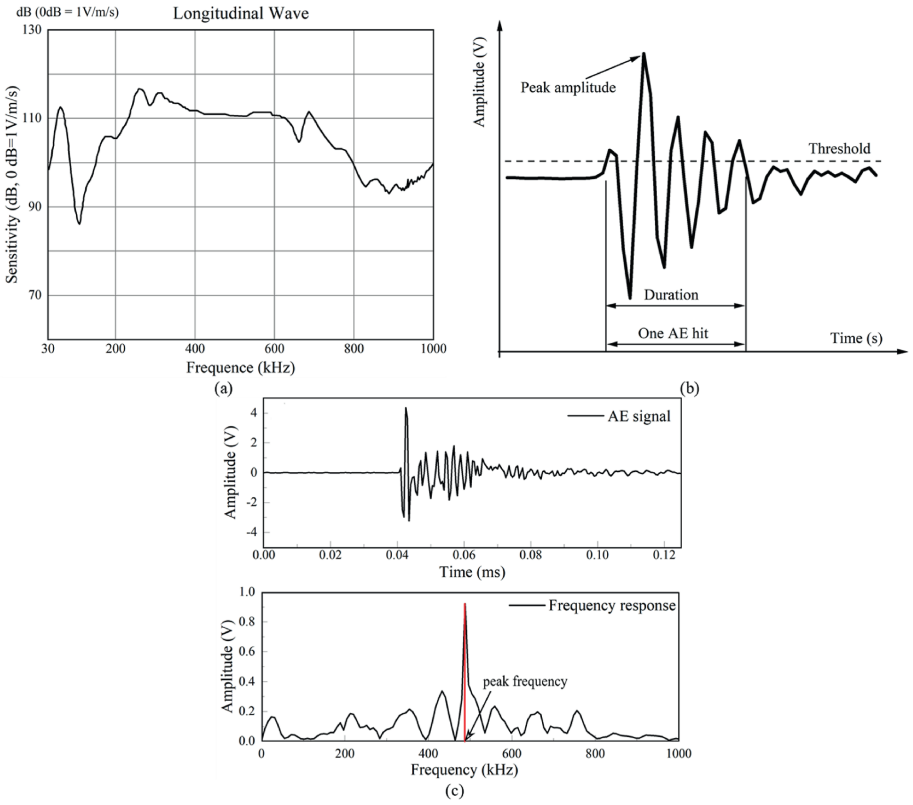

Fig. 4. (a) AE sensor calibration data; (b) A typical AE signal with parameter definition; and (c) The definition of the peak frequency.

Table 3
Specification of the employed AE measurement system.

Type	Feature	Value
AE sensor	Measuring type	Velocity
	Working frequency	10 kHz–5 MHz
	Resonant frequency	240 kHz–360 kHz
	Sensitivity	115 dB ± 3 dB
	Size	5.5 mm × 10 mm (diameter × height)
	Weight	1 g
Main amplifier	Gain	53 dB ± 3 dB
	Frequency range	20–2000 kHz
	Output impedance	75 Ω
Data logger	Maximum analog input (AI) sampling rate	2 MS/s (1-channel)
	AI channels	8 (differential channels)
	AI resolution	16 bits
	Maximum voltage range	−10 V–10 V
	Minimum voltage range	−1 V–1 V

by applying the fast Fourier Transform (FFT) to convert the signal, whereby the frequency component at the spectral peak amplitude was determined (Fig. 4c). This study analyzed the frequency-dependent cumulative AE hits (denoted as D_{AE}) and hit rate (R_{AE}), averaged across eight sensors, to interpret particle interaction behavior. Herein, the AE hit rate is defined as the total number of AE hits recorded over a 10-s interval, aligning with the methodology of prior research (Lin et al., 2020a, 2025). The averaged D_{AE} and R_{AE} are considered appropriate for providing a general and representative overview of the AE information, facilitating comparisons across tests. Given the inherent location-dependent nature of AE data, future work should focus on the dynamic response of individual sensors to accurately correlate measurements with macro-scale soil behavior.

3. Testing results and discussion

3.1. Stress–strain relations of silica sands

Fig. 5 presents the mechanical response of the tested silica sands under varying axial strain (ε_a) and confining stress (σ'_3) levels. The results show typical behaviors, with the deviatoric stress–axial strain (q-ε_a) response varying depending on the failure modes observed. As shown in Fig. 5a, in the absence of shear band formation, the deviatoric stress (q) increases with ε_a, reaching a smooth peak before leveling off, after which the specimen maintains a nearly constant strength over a broad strain range. In contrast, when shear banding is observed, q rises to a distinct peak, followed by significant strain softening. Due to the limitation in

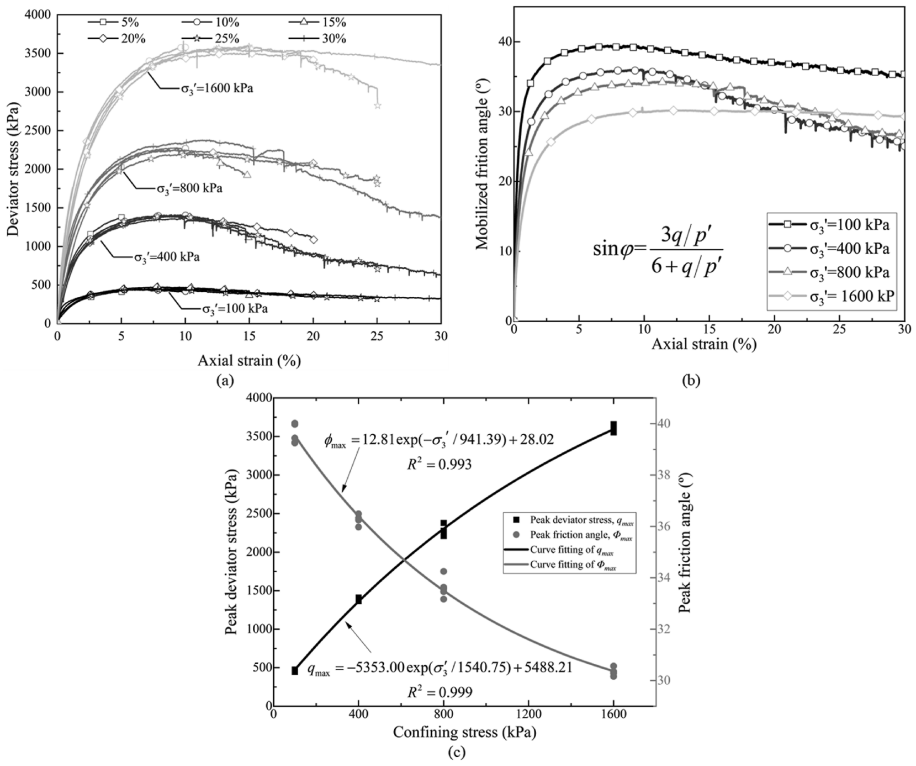

Fig. 5. Mechanical behavior of (a) deviatoric stress with axial strain, (b) sled displacement with axial strain, and (c) mobilized friction angle with axial strain of silica sand No. 3 under different confining stresses in triaxial compression tests.

the applied ε_a, a constant stress, which, along with a constant soil volume, would indicate the arrival of a critical stress state, has not yet been achieved.

The evolution of the mobilized friction angle, with its definition shown in Fig. 5b, with strain follows a trend similar to that of the q-ε_a response. With increasing σ'_3, both the stiffness and strength of the specimen increase (Fig. 5c), while the mobilized friction angle decreases due to particle crushing. Curve fitting of the peak strength and mobilized friction angle reveals that both parameters can be expressed as exponential functions of the confining stress (Fig. 5c), a trend that aligns with established findings (Vesić and Clough, 1968). However, even at the maximum confining stress of 1600 kPa, the "breakdown stress", which is thought to induce the complete breakdown of the interparticle friction angle (Vesić and Clough, 1968), was not reached. This observation suggests that the stress levels applied in this study were insufficient to cause the full fragmentation of the sand particles, indicating a limitation in the stress and strain levels achievable within the experimental setup.

In addition to visual post-test examination of the specimens, evidence for shear band formation is also observed through stress drops (stress relaxation) in the q-ε_a curve. These stress drops are triggered by the stick-slip motion of the unconstrained sled, which, free from lateral restraint (Lin et al., 2021), permits shearing along the developing shear band. Each stress release event is concurrent with a distinct transition in the q degradation pattern, corroborating the shear band formation.

3.2. Particle crushing characterized by B_r

To investigate the particle crushing mechanism, size sieving tests were conducted to obtain the pre- and post-test GSD curves, as shown in Fig. 6a–c. Fig. 6d presents the final GSD curves for all tests in a double-logarithmic scale. For better interpretation, Fig. 7 further illustrates the typical results of the percent finer by weight as a function of 5 % increments in ε_a and σ'_3, presented as bar graphs. Only the results from S3-100 and S3-1600 are shown to illustrate the effect of ε_a on particle crushing in low and high confinement sands (Fig. 7b and c, respectively). Similar trends are observed for the S3-400 and S3-800 tests.

Figs. 6 and 7 show an enhanced generation of grain fragments in the 0.425–2 mm size range. Under low confinement (σ'_3 = 100 kPa), particle crushing mainly generates fragments within the 0.85–2 mm range. In contrast, under high confinement (σ'_3 = 1600 kPa), although fragments mainly fall within the same size range, a significant number of particles smaller than 0.425 mm are also produced due to more pronounced particle crushing (Fig. 7a). This highlights the progressive breakdown of the granular particles and the increasing complexity of the crushing mechanism under different stress and strain levels. It should be emphasized that despite its entrenched role in quantifying particle crushing, sieve analysis suffers from inherent drawbacks in accuracy and comprehensiveness. Common operational artifacts, such as inadequate sieving duration or improper vibration intensity, systematically distort the GSD curve by artificially coarsening or fining the results. These fundamental limitations necessitate developing an advanced measurement system for full-process quantification of particle crushing. The authors address this by developing a frequency-dependent AE parameter-based characterization method, as will be illustrated in the following sections.

Particle crushing of a granular soil assembly would not be an indefinite process, and a stable grading is eventually reached at high stresses (McDowell and Bolton, 1998; McDowell and Harireche, 2002). The result demonstrates that the final GSD curves tend to evolve toward a fractal distribution, evidenced by

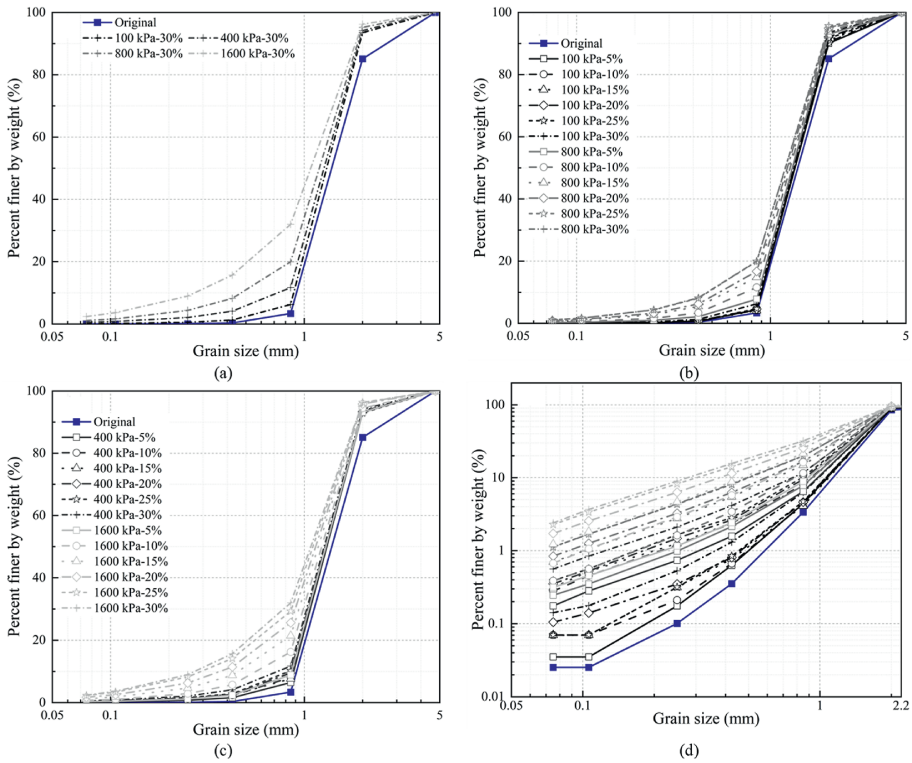

Fig. 6. The pre- and post-test GSD curves for silica sands subjected to (a) confining stress levels of 100 kPa and 800 kPa with strains ranging from 5 % to 30 %, (b) confining stress levels of 400 kPa and 1600 kPa with strains ranging from 5 % to 30 %, (c) confining stress levels of 100–1600 kPa at an axial strain of 30 %, and (d) confining stress levels of 100–1600 kPa with strains ranging from 5 % to 30 % at double-logarithm scale.

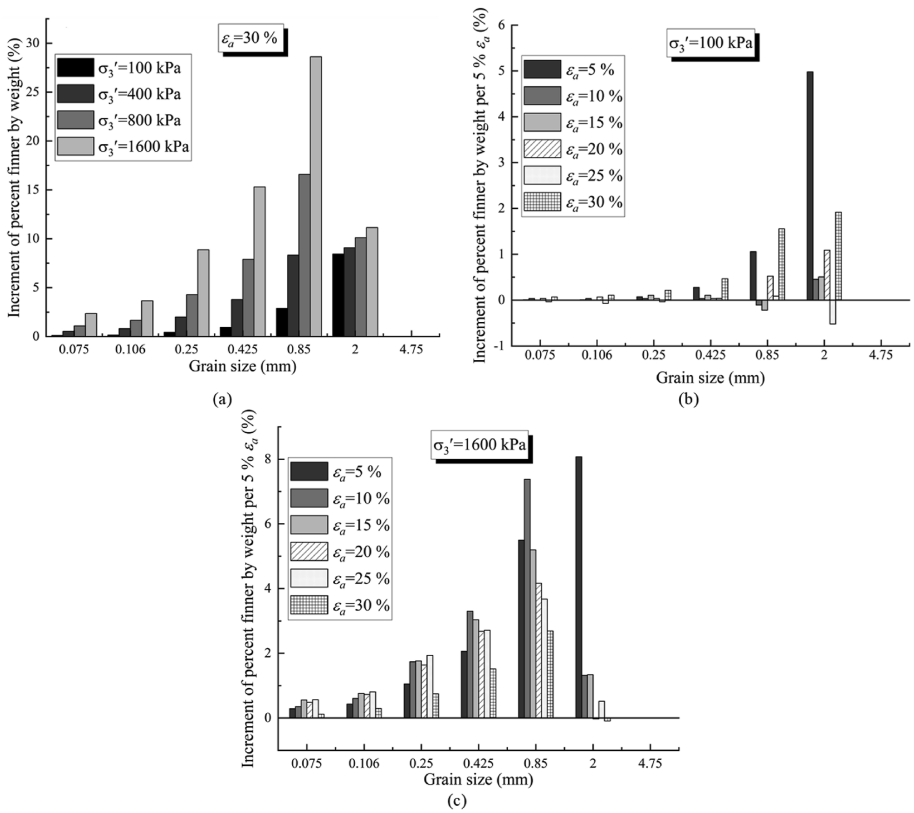

Fig. 7. Typical results of the increment of percent finer by weight with (a) different confining stresses at 30 % axial strain, (b) different axial strain levels at 100 kPa confining stress, and (c) different axial strain levels at 1600 kPa confining stress.

the linear relationship in double-logarithm scale in Fig. 6d, aligning with the findings of earlier studies (Coop et al., 2004; Wang and Yan, 2013). The final GSD curve in this work has a fractal dimension (D) of 1.9 (with the slope (k) of the GSD curves approximately 1.1, and $D = 3 - k$), which aligns with the simulation results reported by Wang and Yan (2013). However, typical fractal dimensions D for many natural soils subjected to crushing are in the range of 2.5–3 (Turcotte, 1986; McDowell and Bolton, 1998), much higher than what was observed here. The relatively smaller D in this study can be attributed to the moderate strain and confining stress levels, which prevent the complete breakdown and fragmentation of the sand particles, resulting in a less pronounced fractal nature of the GSD.

Fig. 8a shows the definition of the relative breakage index, B_r, proposed by Hardin (1985), which was used to quantify the extent of particle crushing. Fig. 8b presents the results of B_r at varying ε_a and σ'_3 levels. The data show that, regardless of the σ'_3 level, B_r increases convexly with increasing strain, showing no sign of stabilization within the stress and strain levels considered. This behavior is consistent with earlier findings (Indraratna and Salim, 2002). Fig. 8c further shows the particle crushing rate per 5 % ε_a (denoted as ΔB_r). In agreement with the trends shown in Figs. 6 and 7, the increase in ΔB_r is rapid during the first 5 % ε_a, followed by a sharp decline in the next 5 %, and then a gradual decrease that eventually stabilizes. The result suggests that the majority of particle crushing occurs within the first 10 % ε_a. Moreover, ΔB_r in high-confinement sands increases faster but decays more slowly with increasing ε_a. Fig. 8d summarizes B_r values at 30 % ε_a (B_r^*) and peak ΔB_r values (ΔB_r^*) as a function of σ'_3. It is found that B_r^* increases nearly linearly with σ'_3, while ΔB_r^* increases rapidly at first but eventually levels off with increasing σ'_3. These results, which are expected to shed valuable light on the fundamental mechanisms governing particle crushing, will be discussed later in detail alongside the corresponding frequency-dependent AE characteristics.

3.3. AE characteristics of silica sands

Our prior review (Lin et al., 2025) established that the frequency content of AE signals effectively distinguishes their source mechanisms in geomaterials. Specifically, in granular soils under low confining stresses (≤80 kPa), AE from particle rearrangement mechanisms like sliding and rolling is characterized by dominant frequencies below 100 kHz, as documented in direct shear and sand avalanche experiments. (Dagois-Bohy et al., 2010; Michlmayr and Or, 2014; Mao and Towhata, 2015; Lin et al., 2019; Liu et al., 2022). On the contrary, particle crushing, particularly catastrophic breakage, generates higher-frequency AE signals (>100 kHz) (Read et al., 1995; He et al., 2010; Mao and Towhata, 2015; Lin et al., 2019). Additionally, prior to catastrophic breakage, particles undergo asperity abrasion and grinding under elevated stresses, especially when surfaces are angular or rough. These interactions produce medium-to-high-frequency AE signals (>100 kHz), as demonstrated by Lin et al. (2019). Similar behavior has been observed in rock shear experiments, where microfractures in brittle asperities and crack ruptures emit high-frequency AE (Ohnaka and Mogi, 1982; Kato et al., 1994). This stress-mediated transition in AE frequency characteristics reflects fundamental changes in energy dissipation mechanisms at particle contacts. The observed frequency shift from predominantly sub-100 kHz signals during particle rearrangement to broadband high-frequency emissions during abrasion, grinding, and fracturing processes provides critical insights for interpreting AE signals in granular systems. Given the mechanistic parallels between asperity/corner breakage and particle crushing, we classify these processes under the broader "crushing condition". Thus, "particle crushing" herein encompasses breakage, asperity abrasion, and grinding. Additional information on AE frequency dependency with particle interactions can be found in Lin et al. (2025).

To ensure consistency with Lin et al. (2025), the AE characteristics were investigated both from the raw data and from high-

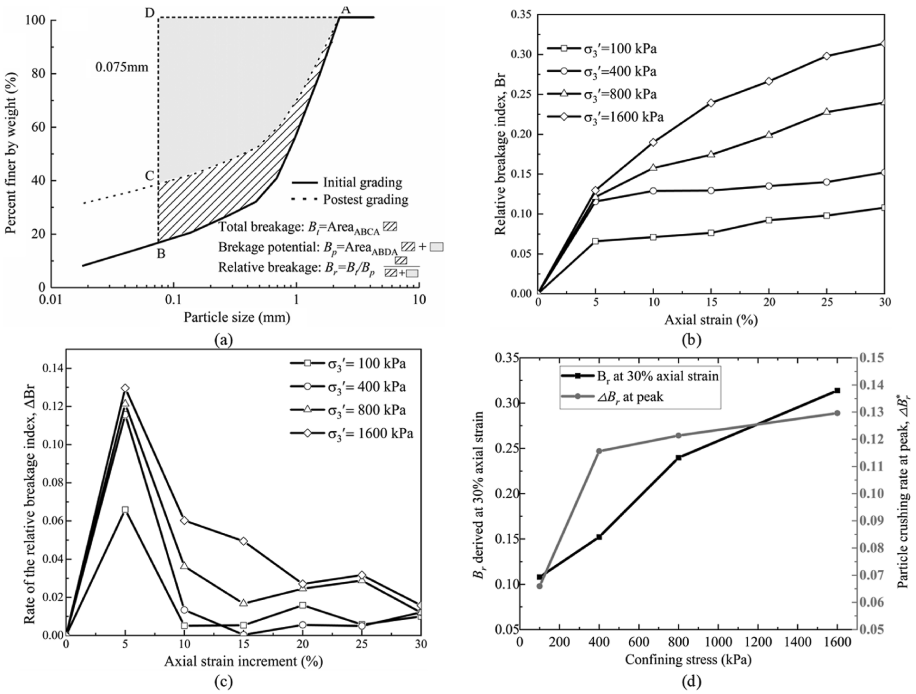

Fig. 8. (a) Definition of relative breakage index, B_r (after Hardin, 1985); (b) Evolution of B_r with strain; (c) Evolution of particle crushing rate (ΔB_r per 5 % axial strain) with strain; and (d) Summarization of B_r^* and ΔB_r^* of silica sands with different confining stresses.

frequency components above 100 kHz that were isolated via Chebyshev high-pass filtering. Fig. 9a and b presents the evolution of cumulative AE hits (D^{T}_{AE}) and the AE hit rate (R^{T}_{AE}) from the raw data, respectively, for the aforementioned tests. The results show good repeatability in the AE responses, with consistency across tests terminated at different prescribed ε_a levels. Consistent with previous findings (Lin et al., 2021), the evolution of the R^{T}_{AE}-ε_a curve closely mirrors the q-ε_a relationship, reflecting the associated failure patterns. That is, without shear banding, the R^{T}_{AE}-ε_a curves are featured with an initial rapid increase followed by a smooth peak and then a quasi-constant regime, whereas the R^{T}_{AE}-ε_a curves with shear banding are featured with an initial rapid increase followed by a gradual increase to a distinct peak and then a gradual decreasing regime. The authors consider that with sufficient strain, R^{T}_{AE} would finally level off, accompanied by the complete formation of a shear band and the arrival of the critical stress state, as observed in our previous results (Lin et al., 2021). Notably, the sudden stress reductions in the q-ε_a curves correlated well with transient decreases in the R^{T}_{AE} curves. This correlation occurs because acoustic waves (so-called stress waves) are intrinsically linked to stress states, where a relationship is quantitatively described by the exponential dependence of AE hit rate on stress intensity factor (Lin et al., 2021).

Fig. 9c summarizes the evolution of D^{T}_{AE} at the end of the test, i.e. at 30 % ε_a (denoted as $D^{T^*}_{AE}$, derived from Fig. 9a) and the peak R^{T}_{AE} (denoted as $R^{T^*}_{AE}$) as a function of σ'_3. The results demonstrate that both $D^{T^*}_{AE}$ and $R^{T^*}_{AE}$ increase exponentially with σ'_3, mirroring the trend observed in the development of peak strength. The findings in Fig. 9 further validate the effectiveness of AE testing in characterizing the shear mechanical properties of sandy soils.

Fig. 10a and b shows the cumulative AE hits (D^{H}_{AE}) and AE hit rate (R^{H}_{AE}) for the high-frequency components (i.e. >100 kHz), respectively. For clarity, the results from the S3-100 case are replotted as insets in both figures. The results reveal a good resemblance between high-frequency AE parameters (i.e. D^{H}_{AE} and R^{H}_{AE}) and particle crushing indices (i.e. B_r and ΔB_r). Both D^{H}_{AE} and R^{H}_{AE} increase with ε_a and σ'_3. Notably, D^{H}_{AE} follows a similar convex increase as B_r with increasing ε_a. Meanwhile, R^{H}_{AE}, which reflects the rate of particle crushing, closely mirrors the evolution of ΔB_r: it rises sharply to a peak and then decreases quickly before leveling off. The turning point of the R^{H}_{AE} curve, marking the most intense particle crushing, occurs at around 2.5 % ε_a. Additionally, as σ'_3 increases, R^{H}_{AE} reaches its peak more rapidly and subsides more slowly during subsequent straining. However, there is an exception with the S3-100 case, where the evolution of D^{H}_{AE} and R^{H}_{AE} diverges from the trends observed for B_r and ΔB_r. This discrepancy is attributed to the different dominant particle crushing modes and potential measurement accuracy issues with B_r, which will be further discussed in the next section.

3.4. Phase validation of the AE feasibility in full-process quantification of particle crushing

Fig. 11 presents the relations between the total cumulative number of high-frequency AE hits ($D^{H^*}_{AE}$) and B_r derived at the prescribed ε_a and varying σ'_3 levels. A linear relationship is established between D^{H}_{AE} and B_r through curve fitting ($R^2 = 0.93$), validating the feasibility of the high-frequency AE signal as a novel and promising parameter to fully quantify a substantial amount of particle crushing of silica sands. Interestingly, for sands subjected

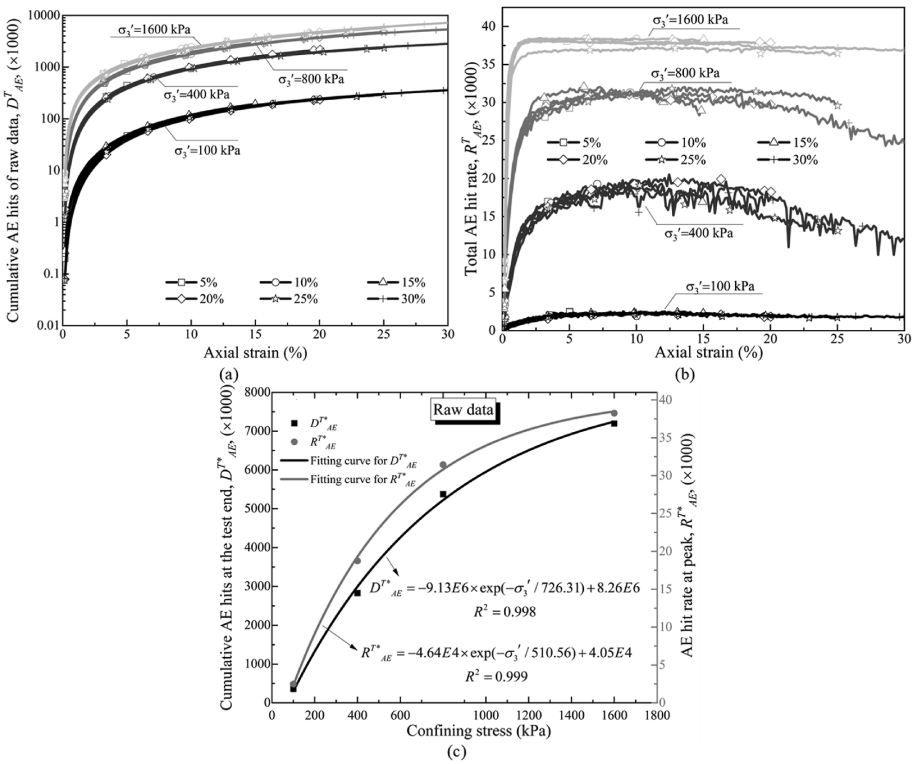

Fig. 9. (a) Cumulative AE hits of the raw data; (b) AE hit rate of the raw data; and (c) Summarization of the total cumulative AE hits at the test end and AE hit rate at the peak of the raw AE data of sands with different confining stresses.

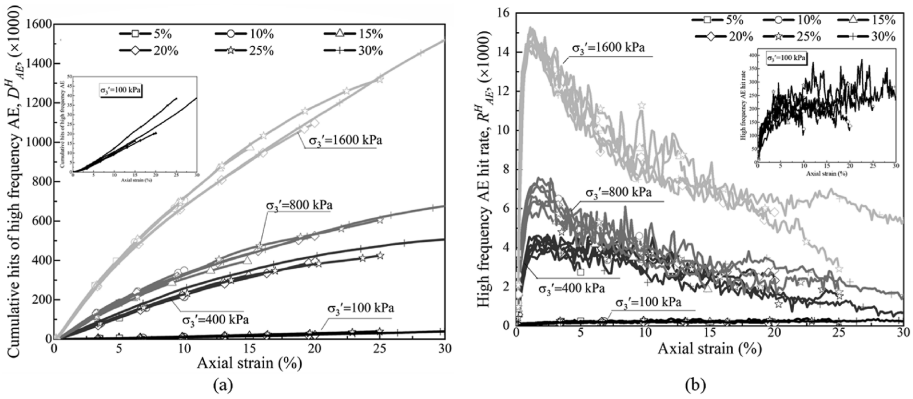

Fig. 10. Evolution of (a) cumulative high-frequency AE hits and (b) high-frequency AE hit rate with axial strain for sands subjected to different confining stresses.

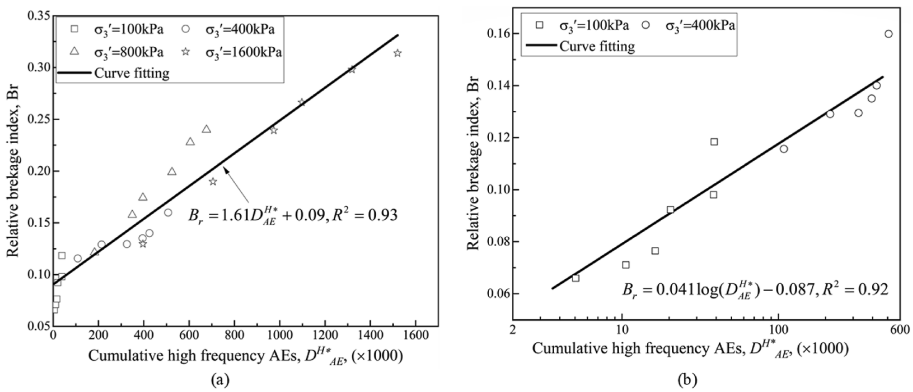

Fig. 11. Relations between the relative breakage index B_r and the cumulative number of high-frequency AE hits $D^{H^*}_{AE}$ for sands subjected to confining stress of (a) 100–1600 kPa and (b)100–400 kPa.

to lower confining stresses (e.g. 100 kPa), B_r exhibits a better fit to a semi-logarithmic relationship with $D^{T^*}_{AE}$ (logarithmic scale), as shown in Fig. 11b, suggesting that the crushing behavior of silica sands under low confinement conditions follows a distinct scaling pattern. This is consistent with our prior work on silica sands with smaller particle sizes and lower confining stresses (Lin et al., 2025). Two primary factors may account for the observed differences in AE responses across sands with varying levels of particle crushing. First, intrinsic differences in the particle crushing modes likely play a role: for a soil assembly with a specific GSD curve, finer silica sands (silica sand No. 5) tend to undergo surface abrasion under lower stresses (as evidenced by Fig. 7b), while larger particles (silica sand No. 3) are more susceptible to corner rupture and particle splitting at higher stresses (as evidenced by Fig. 7c). Second, the B_r index, derived through sieving, may not capture the subtle changes in particle size that occur during the early stages of crushing, particularly at lower confining stresses.

Both GSD-based indices (B_r and ΔB_r) and high-frequency AE signals (D^H_{AE} and R^H_{AE}) confirm that significant particle crushing occurs within the first 5 % ε_a, predominantly increasing particle fragments between 0.425 mm and 2 mm. The rapid increase in D^H_{AE} and R^H_{AE} (or B_r and ΔB_r) during the early shear stages, with a distinct peak in R^H_{AE} at 2.5 % ε_a, highlights the susceptibility of silica sand particles to significant crushing between the yield and peak stresses. This behavior is consistent with observations by McDowell and Harireche (2002) and Wang and Yan (2013), who reported a similar pattern of particle crushing coinciding with the onset of sand yielding. Subsequently, in the post-peak stress regime, the steady increase in D^H_{AE} (or B_r) with ε_a, coupled with the gradual decrease without stabilization in R^H_{AE} (or ΔB_r), suggests that a final stable grading, representing the ultimate state of particle crushing, requires substantial straining, potentially exceeding the strain limit of a typical triaxial test. This finding aligns with the results of Hagerty et al. (1993) and Coop et al. (2004). Additionally, as σ'_3 increases, the initial rapid increase in R^H_{AE} (or ΔB_r) followed by a slight decrease without stabilization indicates that the evolution of particle crushing is stress-state dependent. Higher confining stress leads to a longer period of particle crushing evolution, requiring larger strains to reach the final stable grading in highly confined sands.

3.5. Implication to the nature of particle damage mechanisms by frequency-dependent AE characterization

In addition to the analysis of high-frequency components above 100 kHz, Lin et al. (2019) proposed that analyzing the AE signals across different high-frequency groups can offer additionally valuable insights into the various particle crushing mechanisms involved in the single-particle breakage process. Specifically, different micro-mechanical behaviors during a single-particle breakage, including particle abrasion/grinding, microcracking, and corner breakage/particle splitting, can be distinguished by their characteristic frequency ranges: 100–200 kHz for asperity abrasion/particle grinding, 200–300 kHz for microcracking, and >300 kHz for corner breakage/particle splitting (Lin et al., 2019). The frequency responses associated with single-particle fracturing are illustrated in Fig. 12, with further details provided in Lin et al. (2019). In view of this, we further categorize high-frequency AE signals into three distinct groups — HL (100–200 kHz), HM

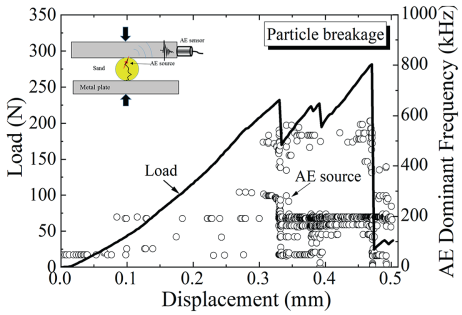

Fig. 12. Typical frequency response of silica sands during single-particle fracturing (after Lin et al., 2019).

(200–300 kHz), and HH (>300 kHz) — and attempt to explore their potential implications for the nature of particle damage mechanisms during shearing.

Fig. 13 presents the AE hit rates for these frequency ranges: R_{AE}^{HL} (100–200 kHz), R_{AE}^{HM} (200–300 kHz), and R_{AE}^{HH} (>300 kHz). To assess the contribution of each frequency group to the overall high-frequency AE signal, Fig. 14 illustrates the ratios of R_{AE}^{HL}, R_{AE}^{HM}, and R_{AE}^{HH} to R_{AE}^{H}, denoted as $\eta_{HL} = R_{AE}^{HL}/R_{AE}^{H}$, $\eta_{HM} = R_{AE}^{HM}/R_{AE}^{H}$, and $\eta_{HH} = R_{AE}^{HH}/R_{AE}^{H}$ ($\eta_{HL} + \eta_{HM} + \eta_{HH} = 1$), respectively, under varying σ_3' levels.

The results reveal that the evolution trends of R_{AE}^{HL} and R_{AE}^{HM} closely mirror the corresponding R_{AE}^{H} curves, irrespective of the σ_3' value. These trends are typically featured with three distinct stages: (1) a rapid increase stage, (2) a transition stage, and (3) a relatively constant or gradually decreasing stage in low-confinement sands (e.g. $\sigma_3' = 100$ kPa) and high-confinement sands (e.g. $\sigma_3' = 1600$ kPa), respectively. In contrast, R_{AE}^{HH} exhibits a distinctive behavior compared to R_{AE}^{H}, particularly in highly confined sands. Its evolution follows a similar three-stage pattern but deviates in the final stage, where it shows a relatively constant or gradually increasing trend under low and high confining stresses, respectively.

For low-confinement sands ($\sigma_3' = 100$ and 400 kPa), R_{AE}^{HL} dominates the total high-frequency AEs throughout the shear process, with η_{HL} decreasing from approximately 0.8 to 0.6 by the end of the test. R_{AE}^{HM} contributes as the second-largest component, with η_{HM} increasing from 0.1 to approximately 0.4. In contrast, R_{AE}^{HH} has the smallest contribution, with η_{HH} remaining between 0.1 and 0.2. As σ_3' increases to 800 kPa, R_{AE}^{HM} becomes the dominant contributor after approximately 3 % ε_a, corresponding to the pre-peak stress regime. In this case, η_{HM} increases from 0.4 to 0.6, while the contribution of R_{AE}^{HL} decreases, with η_{HL} dropping from 0.6 to 0.3. At the highest confining stress ($\sigma_3' = 1600$ kPa), R_{AE}^{HH} initially contributes minimally ($\eta_{HH} \approx 0.05$), but its proportion increases progressively with straining. In the post-peak stress regime, R_{AE}^{HH} slightly surpasses both R_{AE}^{HL} and R_{AE}^{HM}, becoming the dominant contributor, with a final η_{HH} of 0.4.

The above findings imply that during triaxial compression, the evolution of particle crushing processes of silica sands is governed by both the applied confining stress and the progressive strain, resulting in a dynamic transition between different particle damage mechanisms, including particle abrasion/grinding, particle microcracking, and corner breakage/particle splitting. These mechanisms might occur simultaneously but evolve in a stress- and strain-dependent manner, highlighting the progressive failure of the granular assembly. The transition is especially pronounced in high-confinement conditions, where the particle damage mechanism becomes more complex and shifts toward finer particle fragmentation (as evidenced by Fig. 7c). The increased

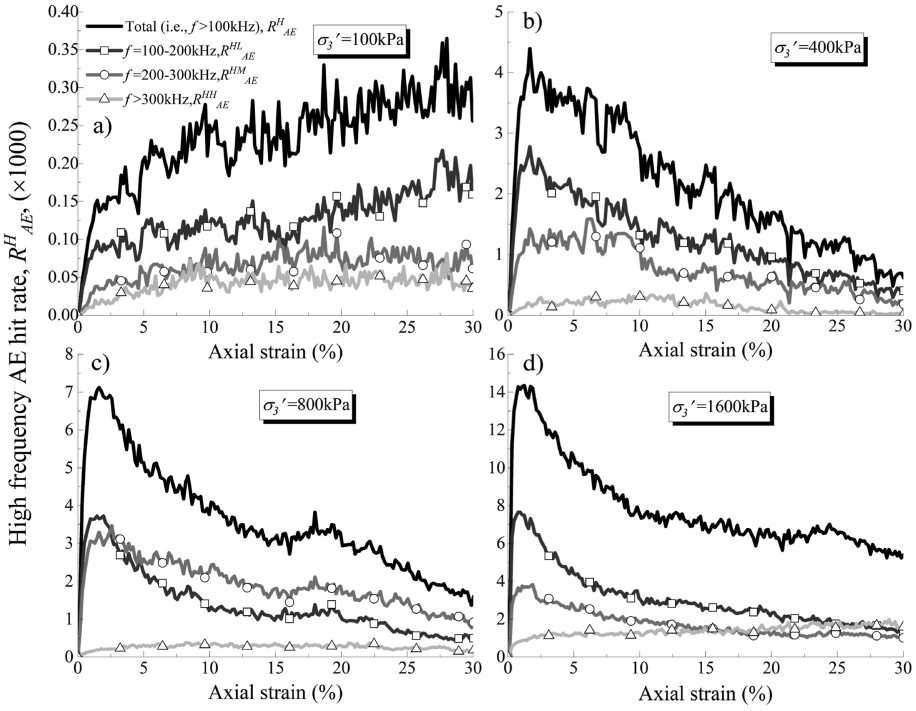

Fig. 13. Evolutions of high-frequency AE hit rate with different frequency groups for silica sands subjected to different confining stresses of (a) $\sigma_3' = 100$ kPa, (b) $\sigma_3' = 400$ kPa, (c) $\sigma_3' = 800$ kPa, and (d) $\sigma_3' = 1600$ kPa in triaxial compression tests.

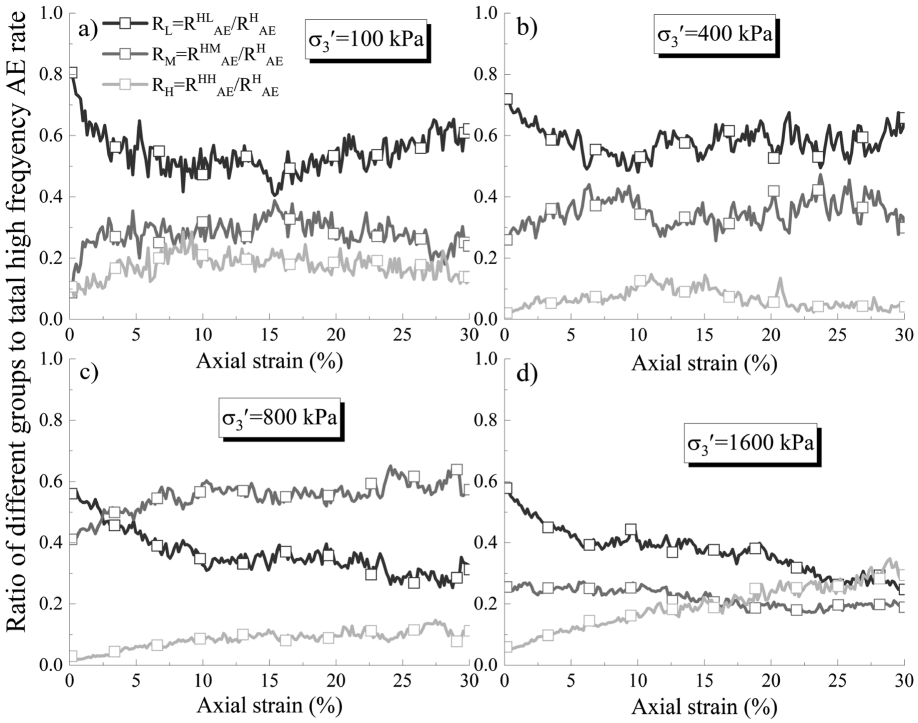

Fig. 14. Ratios of different high-frequency groups to the total high-frequency AEs for silica sands subjected to different confining stresses of (a) $\sigma_3' = 100$ kPa, (b) $\sigma_3' = 400$ kPa, (c) $\sigma_3' = 800$ kPa, and (d) $\sigma_3' = 1600$ kPa in triaxial compression tests.

dominance of higher-frequency AE signals (R^{HH}_{AE}) in Figs. 13 and 14 further underscores the transition of particle damage mechanisms from surface abrasion (R^{HL}_{AE}) and microcracking (R^{HM}_{AE}) to corner breaking and particle splitting (R^{HH}_{AE}), as σ_3' increases. The GSD results presented in Figs. 7 and 8 further corroborate this shift, where an enhanced growth in fragments within the second largest size ranges of 0.855–2 mm occurs in lowly confined sands, while highly confined sands produce a significant number of smaller fragments with sizes smaller than 0.425 mm.

The findings of this study clarify the varying contributions of different particle damage mechanisms, paving the way for more accurate predictions of granular material behavior under various loading conditions. These insights are particularly important for geotechnical applications, such as the design of high embankments, large earth dams, deep soil fills, and other engineering structures, where the material's behavior under high confinement and shear stress directly impacts the stability and safety of the structure. While frequency-dependent AE sources are known to be highly sensitive to testing conditions, such as environmental noise and propagation media. To this end, combining advanced techniques (e.g., DIC, X-ray CT, and DEM simulations) can serve as an alternative to address this gap by capturing particle morphology and micro-mechanical behavior in detail. Such an integrated framework would substantially improve the understanding of the dynamic nature of particle damage evolution, leading to more accurate predictions of granular material response under extreme loading conditions.

4. Conclusions

In this work, a series of stage-experiments of triaxial compression was conducted, incorporating with high-performance AE measurement system, on silica sands with prescribed axial strains and varying confining stresses. After analyzing particle crushing-related parameters of GSD-based indices (i.e. relative breakage index B_r and its rate ΔB_r) and AE-based parameters (i.e. high-frequency AE hits D^{H}_{AE} and hit rate R^{H}_{AE}), some insights regarding the particle crushing mechanism of silica sands upon shearing are offered as follows:

(1) The stage-experimental results phase validates the feasibility of high-frequency AEs (>100 kHz) in the full-process quantification of particle crushing, with a strong linear relation between cumulative AE hits and B_r. However, this linear relation differs from the semi-logarithmic relationship observed at smaller B_r values in previous findings on silica sand, which can be attributed to variations in particle crushing modes and the limitations of B_r measurement.

(2) Both GSD-based indices and AE-based parameters confirm that significant particle crushing occurs early in the initial 5 % of axial strain, corresponding to the yield to peak-stress phase, generating fragments in sizes between 0.425 mm and 2 mm. The steady rise in B_r and D^{H}_{AE}, along with the slower decrease in ΔB_r and R^{H}_{AE} under increased confining stress, suggests that a final stable particle grading requires large strains, potentially beyond the limits of a triaxial test.

(3) The analysis of AE hit rates across different high-frequency groups reveals that R^{HL}_{AE} (100–200 kHz) and R^{HM}_{AE} (200–300 kHz) follow a similar trend to the total R^{H}_{AE} (>100 kHz), while R^{HH}_{AE} (>300 kHz) shows a steady increase under higher confining stresses. This shift suggests a transition toward more complex crushing mechanisms, such as particle abrasion/grinding, and corner breaking/particle splitting. The dominance of specific AE groups at varying

confinement levels underscores the role of confinement in influencing particle crushing behavior.

CRediT authorship contribution statement

Wenli Lin: Writing – review & editing, Methodology, Funding acquisition, Conceptualization. **Shuyu Tian:** Writing – original draft, Investigation, Formal analysis, Data curation. **Deqi He:** Formal analysis, Writing – original draft, Investigation. **Xiao Kang:** Writing – original draft, Investigation, Data curation. **Yuhang Chen:** Writing – original draft, Investigation. **Ang Liu:** Methodology, Conceptualization, Writing – review & editing, Writing – original draft. **Maqsood Zain:** Writing – review & editing, Investigation. **Junichi Koseki:** Writing – review & editing, Supervision.

Declaration of competing interest

The authors declare that they have no known competing financial interests or personal relationships that could have appeared to influence the work reported in this paper.

Acknowledgements

This study was financially supported by the National Natural Science Foundation of China (Grant No.42472347), and the Research Fund for Advanced Ocean Institute of Southeast University (General Program) (Grant No. GP202406). The authors would like to acknowledge the Geotechnical Engineering Laboratory at the University of Tokyo, Japan, for providing testing materials and apparatus used in this research. They also wish to express their sincere appreciation to Mr. Takeshi Sato, formerly of the University of Tokyo, for his exceptional technical support.

Notations

AE	Acoustic emission
GSD	Grain size distribution
B_r	Relative breakage index
B_r^*	B_r values at 30 % axial strain
ΔB_r	Rate of relative breakage index, referring to the rate of particle crushing
ΔB_r^*	Peak value of ΔB_r
D_{50}	Mean particle size
D_{10}	Effective particle size
ε_a	Axial strain
σ_3'	Effective confining stress
q	Deviator stress
p'	Mean effective stress
φ	Mobilized frictional angle
φ_{max}	Maximum mobilized frictional angle
D	Fractal dimension of the final GSD curve
k	Slope of the final GSD curve in double-logarithm scale;
D_{AE}	Cumulative AE hits, in which D_{AE}^T and D_{AE}^H represent those of the raw data and high-pass filtered data, respectively
$D_{AE}^{H^*}$	Total cumulative number of high-frequency AE hits
R_{AE}	AE hit rate, in which R_{AE}^T and R_{AE}^H represent that of the unfiltered data and high-pass filtered data, respectively
R_{AE}^{HL}	AE hit rate in the frequency range of 100–200 kHz
R_{AE}^{HM}	AE hit rate in the frequency range of 200–300 kHz
R_{AE}^{HH}	AE hit rate in the frequency range above 300 kHz
η_{HL}	Ratio of R_{AE}^{HL} to R_{AE}^H
η_{HM}	Ratio of R_{AE}^{HM} to R_{AE}^H
η_{HH}	Ratio of R_{AE}^{HH} to R_{AE}^H

References

Altuhafi, F.N., Coop, M.R., 2011. Changes to particle characteristics associated with the compression of sands. Geotechnique 61 (6), 459–471.
Bandini, V., Coop, M.R., 2011. The influence of particle breakage on the location of the critical state line of sands. Soils Found. 51 (4), 591–600.
Bolton, M.D., Nakata, Y., Cheng, Y.P., 2008. Micro and macro-mechanical behavior of DEM crushable materials. Geotechnique 58 (6), 471–480.
Coop, M.R., Sorensen, K.K., Bodas Freitas, T., Georgoutsos, G., 2004. Particle breakage during shearing of a carbonate sand. Geotechnique 54 (3), 157–163.
Dagois-Bohy, S., Ngo, S., du Pont, S., Douady, S., 2010. Laboratory singing sand avalanches. Ultrasonics 50 (2), 127–132.
Hagerty, M.M., Hite, D.R., Ullrich, C.R., Hagerty, D.J., 1993. One-dimensional high-pressure compression of granular media. J. Geotech. Eng. 119 (1), 1–18.
Hardin, B., 1985. Crushing of soil particles. J. Geotech. Eng. 111 (10), 1177.
He, M.C., Miao, J.L., Feng, J.L., 2010. Rock burst process of limestone and its acoustic emission characteristics under true-triaxial unloading conditions. Int. J. Rock Mech. Min. Sci. 47 (2), 286–298.
Hu, W., Yin, Z., Dano, C., Hicher, P.Y., 2011. A constitutive model for granular materials considering grain breakage. Sci. China Technol. Sci. 54 (8), 2188–2196.
Indraratna, B., Ionescu, D., Christie, H., 1998. Shear behaviour of railway ballast based on large scale triaxial testing. J. Geotech. Geoenviron. Eng. 124 (5), 439–449.
Indraratna, B., Salim, W., 2002. Modelling of particle breakage of coarse aggregates incorporating strength and dilatancy. Geotech. Eng. 155 (4), 243–252.
JGS 0111, 2015. Test Method for Density of Soil Particles. Japanese Geotechnical Society, Tokyo, Japan.
JGS 0131, 2015. Test Method for Particle Size Distribution of Soils. Japanese Geotechnical Society, Tokyo, Japan.
JGS 0161, 2015. Test Method for Minimum and Maximum Densities of Sands. Japanese Geotechnical Society, Tokyo, Japan.
Kato, N., Yamamoto, K., Hirasawa, T., 1994. Microfracture processes in the breakdown zone during dynamic shear rupture inferred from laboratory observation of near-fault high-frequency strong motion. Pure Appl. Geophys. 142 (3–4), 713–734.
Kong, X., Liu, J., Zou, D., Liu, H., 2016. Stress-dilatancy relationship of Zipingpu gravel under cyclic loading in triaxial stress states. Int. J. GeoMech. 16 (4), 04016001.
Kundu, T., 2014. Acoustic source localization. Ultrasonics 54 (1), 25–38.
Lade, P.V., Nam, J., Liggio Jr, C.D., 2010. Effects of particle crushing in stress drop-relaxation experiments on crushed coral sand. J. Geotech. Geoenviron. Eng. 136 (3), 500–509.
Lade, P.V., Yamamuro, J.A., Bopp, P.A., 1996. Significance of particle crushing in granular materials. J. Geotech. Geoenviron. Eng. 122 (4), 309–316.
Lee, K., Farhoomand, I., 1967. Compressibility and crushing of granular soil in anisotropic triaxial compression. Can. Geotech. J. 4 (1), 68–86.
Lei, X., Masuda, K., Nishizawa, O., Jouniaux, L., 2004. Detailed analysis of acoustic emission activity during catastrophic fracture of faults in rock. J. Struct. Geol. 26 (2), 247–258.
Li, S., Smith, A., 2025. Pipeline–soil interaction behavior: acoustic emission and energy dissipation. J. Geotech. Geoenviron. Eng. 151 (2), 04024157.
Li, Z., Zhang, Y., Chen, R., Tai, P., Zhang, Z., 2025. Numerical investigation of morphological effects on crushing characteristics of single calcareous sand particle by finite-discrete element method. Powder Technol. 453, 120592.
Li, Z., Zhang, Z., Tai, P., Shen, P., Li, J., 2024. Investigation of morphological effects on crushing characteristics of calcareous sand particle by 3D image analysis with spherical harmonics. Powder Technol. 433, 119204.
Lin, W., Liu, A., Mao, W., 2019. Use of acoustic emission to evaluate the micro-mechanical behavior of sands in single particle compression tests. Ultrasonics 99, 105962.
Lin, W., Liu, A., Mao, W., Koseki, J., 2020b. Acoustic emission behavior of granular soils with various ground conditions in drained triaxial shearing tests. Soils Found. 60 (4), 929–943.
Lin, W., Liu, A., Mao, W., Koseki, J., 2020a. Acoustic emission characteristics of a dry sandy soil subjected to drained triaxial compression. Acta Geotech. 15, 2493–2506.
Lin, W., Liu, A., Mao, W., Koseki, J., 2025. Frequency dependence of acoustic emission with particle interaction and failure process in dry sands during triaxial compression. Geotechnique 75, 1–15.
Lin, W., Liu, A., Zhang, E., Tian, S., He, D., 2024a. Effect of cementation on the mechanical response of sands using acoustic emission technique. Geotechnique 75, 582–594.
Lin, W., Liu, A., Zhang, E., Tian, S., He, D., Maqsood, Z., 2024b. Macro-micro mechanical behavior of saturated cemented sands during drained triaxial shearing. Constr. Build. Mater. 434, 136787.
Lin, W., Mao, W., Liu, A., Koseki, J., 2021. Application of an acoustic emission source-tracing method to visualise shear banding in granular materials. Geotechnique 71, 925–936.
Liu, H., Zou, D., 2013. Associated generalized plasticity framework for modeling gravelly soils considering particle breakage. J. Eng. Mech. 139 (5), 606–615.
Liu, H., Zou, D., Liu, J., 2014. Constitutive modeling of dense gravelly soils subjected to cyclic loading. Int. J. Numer. Anal. Methods GeoMech. 38 (14), 1503–1518.
Liu, Z.M., Jiang, Y., Wang, D.J., Fu, Y.J., 2022. Four types of acoustic emission characteristics during granular stick-slip evolution. J. Mt. Sci. 19 (1), 276–288.

Mandelbrot, B.B., 1983. The Fractal Geometry of Nature. W.H. Freeman and Company, New York, USA.
Manuello, A., Gianni, N., Alberto, C., 2019. AE monitoring of a concrete arch road tunnel: damage evolution and localization. Eng. Fract. Mech. 210, 279–287.
Mao, W., Towhata, I., 2015. Monitoring of single-particle fragmentation process under static loading using acoustic emission. Appl. Acoust. 94, 39–45.
Mao, W., Pan, L., Yang, Y., Zheng, H., Huang, Y., 2025. Particle breakage and acoustic emission characteristics of granular soils under large shear deformation. Acta Geotech. 20, 3773–3793.
Mao, W., Yang, Y., Lin, W., Aoyama, S., Towhata, I., 2018. High frequency acoustic emissions observed during model pile penetration in sand and implications for particle breakage behavior. Int. J. GeoMech. 18 (11), 04018143.
Marsal, R.J., 1967. Large scale testing of rockfill materials. J. Soil Mech. Found. Div. ASCE 93 (2), 27–43.
McDowell, G.R., Harireche, O., 2002. Discrete element modelling of yielding and normal compression of sand. Geotechnique 52 (4), 299–304.
McDowell, G.R., Bolton, M.D., 1998. On the micromechanics of crushable aggregates. Geotechnique 48 (5), 667–679.
McDowell, G.R., Bolton, M.D., Robertson, D., 1996. The fractal crushing of granular materials. J. Mech. Phys. Solid. 44 (12), 2079–2102.
Michlmayr, G., Or, D., 2014. Mechanisms for acoustic emissions generation during granular shearing. Granul. Matter16 (5), 627–640.
Miura, N., O-Hara, S., 1979. Particle crushing of a decomposed granite soil under shear stresses. Soils Found. 19 (3), 1–14.
Nakata, Y., Hyde, A.F.L., Hyodo, M., Murata, H., 1999. A probabilistic approach to sand particle crushing in the triaxial test. Geotechnique 49 (5), 567–583.
Nakata, Y., Hyodo, M., Hyde, A.F.L., Kato, Y., Murata, H., 2001. Microscopic particle crushing of sand subjected to high pressure one-dimensional compression. Soils Found. 41 (1), 69–82.
Ohnaka, M., Mogi, K., 1982. Frequency characteristics of acoustic emission in rocks under uniaxial compression and its relation to the fracturing process to failure. J. Geophys. Res. Solid Earth 87 (B5), 3873–3884.
Peng, Y., Yin, Z.Y., Ding, X., 2022. Analysis of particle corner-breakage effect on pile penetration in coral sand: model tests and DEM simulations. Can. Geotech. J. 60 (5), 749–765.
Read, M., Ayling, M., Meredith, P., Murrell, S., 1995. Microcracking during triaxial deformation of porous rocks monitored by changes in rock physical properties, II. Pore volumometry and acoustic emission measurements on water-saturated rocks. Tectonophysics 245 (3), 223–235.
Smith, A., Dixon, N., 2019. Acoustic emission behaviour of dense sands. Geotechnique 69 (12), 1107–1122.
Turcotte, D.L., 1986. Fractals and fragmentation. J. Geophys. Res. 91 (B2), 1921–1926.
Tyler, S.W., Wheatcraft, S.W., 1992. Fractal scaling of soil particle-size distributions: analysis and limitations. Soil Sci. Soc. Am. J. 56 (2), 362–369.
Vesić, A.S., Clough, G.W., 1968. Behavior of granular materials under high stresses. J. Soil Mech. Found. Div. ASCE 94 (3), 661–688.
Wang, J., Yan, H., 2013. On the role of particle breakage in the shear failure behavior of granular soils by DEM. Int. J. Numer. Anal. Methods GeoMech. 37 (8), 832–854.
Xiao, Y., Liu, H., 2017. Elastoplastic constitutive model for rockfill materials considering particle breakage. Int. J. GeoMech. 17 (1), 04016041.
Yao, C., He, C., Takemura, J., Feng, K., Guo, D., Huang, X., 2021b. Active length of a continuous pipe or tunnel subjected to reverse faulting. Soil Dynam. Earthq. Eng. 148, 106825.
Yao, C., Takemura, J., Guo, W., Yan, Q., 2021a. Hyperbolic spiral model for predicting reverse fault ruptures in sand based on centrifuge tests. Geotechnique 71 (7), 571–582.
Yao, C., Zhang, Y., He, C., Yang, W., Yan, Q., Guo, D., 2023. New insights into normal fault rupture propagation in sand. Acta Geotech. 18 (7), 3435–3449.
Yao, T., Cao, Z., Li, W., 2024. On the mechanical behaviour of a coral silt from the South China Sea. Geotechnique 75 (5), 698–711.
Yao, T., Li, W., 2023. Effect of initial fabric from sample preparation on the mechanical behaviour of a carbonate sand from the South China Sea. Eng. Geol. 326, 107311.
Yu, F., 2017c. Particle breakage and the drained shear behavior of sands. Int. J. GeoMech. 17 (8), 04017041.
Yu, F.W., 2017b. Characteristics of particle breakage of sand in triaxial shear. Powder Technol. 320, 656–667.
Yu, F.W., 2017a. Particle breakage and the critical state of sands. Geotechnique 67 (8), 713–719.
Yu, F.W., 2018. Particle breakage in triaxial shear of a coral sand. Soils Found. 58 (4), 866–880.

Dr. Ang Liu is an Associate Professor at the School of Transportation Engineering, Nanjing Tech University, China. He holds dual PhD degrees in Geological Engineering from Tongji University, China, and Intelligent Mechanical Systems from Tokushima University, Japan. His research interests include time-dependent mechanical behavior and constitutive modeling of rocks, macro- and micro-scale mechanical properties of granular materials, and acoustic emission-based intelligent sensing in geotechnical engineering. Specializing in geotechnical testing and numerical simulation, Dr. Liu has developed particular expertise in stress relaxation behavior, soil–structure interaction, and particle breakage mechanisms in geomaterials.